# Sensitivity of the Shallow-to-Deep Convective Transition to Moisture and Wind Shear in the Amazon

**Leandro Alex Moreira Viscardi[1,2], Giuseppe Torri[2], David Kenton Adams[3], and Henrique de Melo Jorge Barbosa[1,4]**

[1]Institute of Physics, University of São Paulo, São Paulo, SP, Brazil
[2]Department of Atmospheric Sciences, University of Hawai'i at Mānoa, Honolulu, HI, USA
[3]El Instituto de Ciencias de la Atmósfera y Cambio Climático, Universidad Nacional Autónoma de México, Mexico City, Mexico
[4]Physics Department, University of Maryland Baltimore County, Baltimore, MD, USA

**Key Points:**

- SAM-LSM consistently reproduces the GoAmazon2014/5 observations for precipitation, moisture, and surface fluxes during the wet season.
- Daytime convection shows a noticeable sensitivity to pre-convective low-level humidity and a weaker response to free troposphere humidity.
- Vertical wind shear has a lesser influence than humidity on the shallow-to-deep convective transition.

Corresponding author: Leandro Viscardi, viscardi@hawaii.edu

## Abstract

Deep convection is the primary influence on weather and climate in tropical regions. However, understanding and simulating the shallow-to-deep (STD) convective transition has long been challenging. Here, we conduct high-resolution numerical simulations to assess the environmental controls on the evolution of isolated convection in the Amazon during the wet season. Observations and large-scale forcing derived through the constrained variational analysis approach for the GoAmazon2014/5 experiments are used in the simulations and model validation. The model consistently reproduces the GOAmazon observations for precipitation, moisture, and surface fluxes of radiation, latent and sensible heat. Through sensitivity experiments, we examine the relative importance of moisture and vertical wind shear in controlling the STD convective transition. Reducing the pre-convective humidity within the lower 1.5 km significantly suppresses vertical development and lowers the ice water path. Additionally, the maximum precipitation rate decreases almost quadratically with column water vapor. Conversely, a reduction of column water vapor above 1.5 km by a factor of two or more is necessary to produce a comparable decrease in ice water path or precipitation. Moderate low-level wind shear facilitates the STD transition, leading to an earlier peak of ice water compared to stronger wind shear or its absence. Although upper-level wind shear negatively influences high cloud formation, its role in controlling the STD transition is relatively smaller than that of low-level wind shear. Our results help quantify the role of moisture and wind shear on the STD transition, but also suggest that dynamic factors may exert a more pronounced influence.



## Plain Language Summary

The Amazon rainforest plays a vital role in the Earth's climate system. However, it is not entirely understood how environmental conditions control the evolution from fair weather conditions to severe thunderstorms in regions of the deep Tropics. We address this problem utilizing numerical simulations that capture the interactions between the forest, atmosphere, and clouds. Atmospheric modeling data developed for the GoAmazon2014/5 experiment are used to initialize our Amazon-based simulations. The model consistently reproduces the Amazon environment throughout the period of our simulations, which covers December 2014. Additionally, we contrast the model results between the control simulation and experiments in which the moisture or wind is modified to evaluate their relative importance to cloud development and precipitation. Lower tropospheric moisture is critical to cloud growth. The amount of moisture in the air above 1.5 km has a minor contribution to cloud development and precipitation. Low-level wind of moderate strength facilitates cloud development during the afternoon. The upper-level wind negatively affects the ice formation in high clouds. These results help strengthen our knowledge of tropical convection, critical for improving numerical model performance.


## 1 Introduction

Deep convection dominates the weather and climate in the tropics. Nevertheless, comprehending and simulating the convective processes is a formidable challenge due to the wide range of spatial and temporal scales involved (Mapes et al., 2009; Moncrieff et al., 2012; Zhang et al., 2013). Shallow cumulus convection, a small-scale phenomenon lasting tens of minutes and covering spatial scales of the order of a few kilometers, oftentimes evolves into deep convective clouds covering tens of kilometers within typical time scales of 2 to 4 hours (Wu et al., 2009; Hohenegger & Stevens, 2013; Adams et al., 2013; Henkes et al., 2021; Powell, 2022). Moreover, deep convection frequently becomes organized and experiences upscale growth into mesoscale convective systems (MCSs) with lifetimes spanning hours to a day and ranging in horizontal scale from 100 km to 1,000 km (Houze Jr, 2004). Likewise, land-atmosphere interactions and complex physical pro-

cesses ranging from cloud microphysics to the generation of gravity waves are intrinsically tied to deep convection (Silva Dias et al., 2002; Mapes et al., 2006; Mapes & Neale, 2011; Jewtoukoff et al., 2013; Gupta et al., 2023).

General circulation models (GCMs) rely on parameterizations of convective processes and typically struggle to reproduce the shallow-to-deep (STD) convective transition over continental regions (Betts, 2002; Betts & Jakob, 2002; Bechtold et al., 2004; Grabowski et al., 2006). Their simulated precipitation peaks much earlier than observed (Lin et al., 2000; Betts, 2002; Collier & Bowman, 2004; Dai & Trenberth, 2004), which is an important source of bias and uncertainty in GCMs to this day (Sherwood et al., 2014; Stevens & Bony, 2013; Itterly et al., 2018; Maher et al., 2018; Freitas et al., 2020, 2024). To circumvent the inherent challenges posed by convective parameterizations, cloud-resolving models (CRMs), which explicitly resolve the up- and downdrafts in clouds, have been used to study convective processes over continental and oceanic regions. For example, M. Khairoutdinov and Randall (2006) conducted the first high-resolution numerical simulations to investigate the STD transition over the Amazon. Their findings highlighted the importance of cold pools in forcing the development of deep convection, while the impact of vertical wind shear and free tropospheric preconditioning were relatively minor. As part of the EUROCS (EUROpean Cloud Systems study), Derbyshire et al. (2004) evaluated the sensitivity of cumulus convection to free tropospheric humidity. Unlike M. Khairoutdinov and Randall (2006), they observed intense deep precipitating convection in moister scenarios, whereas only shallow convection was evident in the driest scenario. Waite and Khouider (2010) conducted idealized numerical simulations over the tropical Atlantic Ocean. Their study emphasized the importance of congestus preconditioning, which reduces the impact of entrainment on cloud buoyancy, ultimately leading to the STD transition. In contrast, Hohenegger and Stevens (2013) showed that the transition from congestus to deep convective clouds occurs on shorter time scales than required for congestus clouds to moisten the atmosphere sufficiently. This implies that dynamic factors play a more substantial role in driving convection. While CRM studies offer valuable insights into physical convective processes, they still require validation through high-resolution observations, which have typically been lacking in tropical rainforests.

In the Amazon, important, but often limited field campaigns, have explored different aspects of tropical convection. Adams et al. (2015) established the Amazon Dense GNSS Meteorological Network, a one-year campaign to observe the interaction between water vapor fields and deep convection. Adams et al. (2013) also utilized GNSS/GPS data from a long-term single site (July 2008 to December 2011) in Manaus, Brazil to evaluate the water vapor convergence associated with the STD transition and found a weak and quasi-linear convergence timescale of approximately 8 hours, followed by a robust and non-linear convergence timescale of approximately 4 hours during the STD transition. Later, Adams et al. (2017) employed this dense network data to investigate how vapor fields evolve spatially during during the STD transition. Their results were consistent with the 4-hour STD timescale and the spatial evolution was reflective of the water vapor convergence posited in the single site study. More recently, the Green Ocean Amazon (GOAmazon) 2014/5 Experiment (Martin et al., 2016, 2017) was carried out from 2014 to 2015 in the central Amazon, providing the most comprehensive set of observations of clouds and aerosols in the Amazon to date. Analyzing this dataset during the dry season (June-September), Ghate and Kollias (2016) noted an excess of water vapor above 2 km during the early morning when contrasting locally-driven precipitating days and nonprecipitating days. Conversely, Zhuang et al. (2017) and Tian et al. (2021) observed that deep convective days exhibit relatively higher moisture extending from the surface to mid-levels in all seasons. Schiro et al. (2016) showed a robust correlation between total column water vapor and precipitation in both the central Amazon and the tropical western Pacific. Furthermore, Schiro and Neelin (2019) demonstrated a strong connection between the initiation and likelihood of daytime precipitation and the bound-

ary layer and lower free troposphere moisture content. Previous studies do not completely agree on the relative importance of vertical wind shear. For example, while Zhuang et al. (2017) indicated that more intense low-level and deep-layer bulk wind shears facilitate the STD transition during the dry season (June-September), Chakraborty et al. (2018) suggested that a more intense low-level shear could inhibit deep convection during the transition season (August–November), especially if it increases the entrainment of dry air.

In this paper, we conduct high-resolution model simulations to assess the role of moisture and vertical wind shear in controlling the STD convective transition in the Amazon. First, we focus on model validation employing GoAmazon data for the period of December 2014. Then, we conduct idealized sensitivity experiments in which either moisture or large-scale wind are modified at different atmospheric levels to assess their relative importance in the development of deep convection. The paper is structured as follows: Section 2 shows the study area. Section 3 describes the material and methods. Section 4 covers the model validation. Sensitivity experiments for moisture and wind shear are conducted in section 5. A discussion of the results is given in section 6. Section 7 contains the conclusions.

## 2 Study Region

The Amazon Basin is bordered by significant altitudes (Figure 1a), primarily in the western region, where some peaks in the Andes Mountains rise well over 6,000 meters in elevation above sea level. However, the simulations are conducted over the GoAmazon2014/5 campaign region in the central Amazon, where the topography can be adequately considered as an extensive plain with minimal variations ($< 130$ m in our domain of interest, section 3.2). During the experiment, most of the observations were taken from the T3 site, located 70 km downwind of Manaus, in Manacapuru (3.21°S, 60.60°W), a site characterized by a pasture surrounded by forest and close to the intersection of the Solimões River and Negro River (Figure 1b).

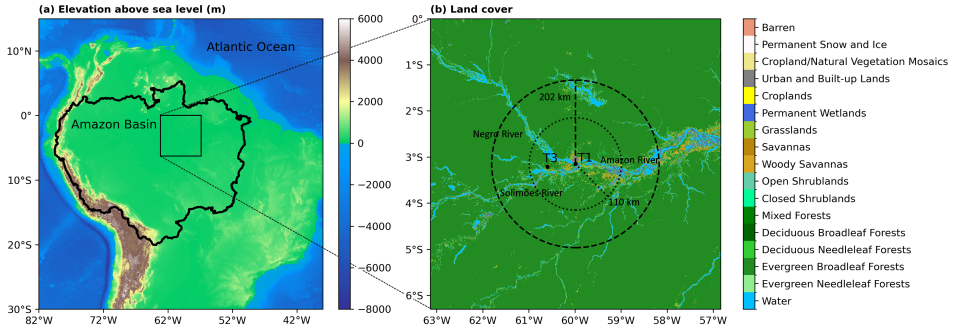


**Figure 1.** (a) Land topography and ocean depth (NOAA National Centers for Environmental Information, 2022) around the Amazon. (b) Land cover (Friedl et al., 2010) around the GoAmazon2014/5 sites. The dashed circle with a radius of 202 km centered at the T1 site (in Manaus) corresponds to the S-band radar domain. The dotted circle with a radius of 110 km shows the domain of the large-scale forcing developed for the GoAmazon2014/5 Experiment (Tang et al., 2016). We also indicate the Amazon, Solimões, and Negro Rivers on the map. Land cover is from 2014, based on the Moderate Resolution Imaging Spectroradiometer (MODIS) - International Geosphere-Biosphere Programme (IGBP) land cover classification system. The Amazon Basin contour is provided by Mayorga et al. (2012).

# 3 Material and Methods

## 3.1 Data

For model validation, we use campaign observations of precipitation, moisture, radiation, and surface latent and sensible heat fluxes. Precipitation is based on the SIPAM S-band radar measurements (Schumacher & Funk, 2018), which we average over the domain of the control runs. Sensible heat flux (H) and latent heat flux (LE) are from the Quality Controlled Eddy Correlation (QCECOR) Flux Measurement (ARM, 2014b). Surface radiation fluxes are from the Sky Radiation Radiometers (SKYRAD) and Ground Radiation Radiometers (GNDRAD) (ARM, 2013). Column water vapor (CWV) is calculated from the balloon-borne sounding system (SONDE), which provides the vertical profiles of thermodynamic conditions 4 times per day during the period of this study, at 02, 08, 14, and 20 LST (ARM, 2014a).

Large-scale atmospheric fields of water vapor mixing ratio, temperature, wind, and moisture and temperature tendencies are based on 3-hour Constrained Variational Analysis Data (VARANAL). This assimilation product was developed using atmospheric fields from the European Centre for Medium-Range Weather Forecasts (ECMWF) ERA-Interim reanalysis (Dee et al., 2011), which were mainly constrained by the SIPAM S-band radar precipitation rate and ARM surface fluxes through the column heat and moisture budget analysis (Tang et al., 2016). The VARANAL data represent an average over the analysis domain centered at T1 site, covering a radius of 110 km (Figure 1b).

The Moderate Resolution Imaging Spectroradiometer (MODIS) provides data products of land cover type (MCD12Q1 Version 6) and leaf area index (MCD15A2H Version 6.1) (Friedl et al., 2010). Specifically, we use the land cover product based on the International Geosphere-Biosphere Programme (IGBP) land cover classification system. Silt, clay, and sand content in the soil are based on in-situ measurements of the soil type "Terra Firme" (Terra-firma) described in Table 1 on Schaefer et al. (2017). Soil temperature and wetness are based on the NASA Global Land Data Assimilation System (GLDAS) Noah Land Surface Model L4 3 hourly 0.25 x 0.25 degree V2.1 (Rodell et al., 2004).

## 3.2 Model Configuration

We employ the numerical model System for Atmospheric Modeling (SAM), version 6.11.8, which solves the anelastic equations of motion and uses liquid water static energy, total nonprecipitating, and precipitating water as thermodynamic prognostic variables (M. F. Khairoutdinov & Randall, 2003). The equations are solved using lateral periodic boundary conditions. A prognostic turbulent kinetic energy 1.5-order closure scheme is used to parameterize subgrid-scale effects. Different microphysics parameterizations are available, including the single-moment (Morrison, 2003), double-moment (Morrison et al., 2005), and Predicted Particle Properties (P3) (Morrison & Milbrandt, 2015) schemes. The radiative heating can be prescribed or calculated by choosing a radiation scheme, either the Community Atmosphere Model (CAM3) (Collins et al., 2006) or the Rapid Radiative Transfer Model (RRTM) (Mlawer et al., 1997) schemes. Surface fluxes can be prescribed or calculated using Monin-Obukhov similarity theory or a simplified Land Surface Model (LSM) (Lee & Khairoutdinov, 2015), which is only compatible with the CAM3 radiation scheme for the current SAM-LSM version.

The baseline configuration for the simulations analyzed in this paper considers a domain of $200\times200\times27$ km$^3$. This choice was made primarily to reasonably accommodate MCSs, given that they typically span about 100 km (Houze Jr, 2004). The horizontal resolution is 500 m, and the vertical resolution varies: it starts at a minimum of 50 m below 1.5 km and increases to 300 m in the upper troposphere. From there, it gradually stretches up to 500 m at the model's upper boundary, which reaches 27 km, resulting in 128 vertical levels. The temporal resolution is 5 seconds, and instantaneous model

fields and statistics are output every 30 minutes. The control simulation uses the P3 microphysics scheme. The CAM3 radiation scheme is called every 150 seconds. Surface fluxes are calculated through the LSM (see Section 3.3).

The large-scale forcing is based on the VARANAL dataset for the period of December 2014 in the central Amazon. Winds were nudged with a 2-hour timescale throughout the simulation. The water vapor mixing ratio was nudged only during the spin-up, considered as the period from 1-5 December 2014, with a timescale of 6 hours.

For the purpose of model validation, we conducted additional simulations where the only modificatio was the choice of the microphysics scheme: single-moment, double-moment, or P3 schemes. We also assessed model sensitivity to resolution and domain size by performing additional simulations at 250 m resolution or with a $400\times400\times27$ km$^3$ domain.

### 3.3 Land Surface Model Configuration

The simplified Land Surface Model uses a minimalist set of parameters to solve the transport of heat, moisture, and radiation in the soil and vegetation and calculate the transfer of momentum between the surface and the atmosphere (Lee & Khairoutdinov, 2015). It adequately idealizes the land-atmosphere interactions, which fundamentally influence convection over the Amazon forest (Silva Dias et al., 2002; Betts, 2002). To define the characteristics of the surface and the vegetation for the LSM, we use the MODIS data of land cover type during 2014 and mean leaf area index (LAI) for December 2014 over a domain of $200\times200$ km$^2$ centered at T3 site (see Figure S1). These are associated with the period and area of our simulations. The surface LAI was set to 4.4 m$^2$ m$^{-2}$, which corresponds to the domain average in satellite observations. In addition, we choose to cover the surface uniformly with evergreen broadleaf forests, which cover 83% of the area in observations. However, based on several tests conducted to optimize the LSM parameters, we modify the default near-infrared visible albedo for vegetation from 0.20 to 0.30, the root length from 150 cm to 200 cm, and the displacement height factor from 0.68 to 0.65. The corresponding displacement height is $0.65 \times 20$ m $= 13$ m, where 20 m is the default value of the height of the canopy. These modifications improve the agreement between the observations and the simulated surface radiation, latent and sensible heat fluxes.

The soil is simulated using 11 layers from the surface down to a depth of 400 cm. Clay and sand contents for each layer are based on in-situ measurements on Terra-firma forests (section 3.1). The initial conditions for soil temperature and soil wetness are based on GLDAS Noah, which provides information on 4 layers: 0-10, 10-40, 40-100, and 100-200 cm. The LSM soil layers close to the surface, which experience greater diurnal cycle variation, are interpolated using the nearest neighbor method. The deeper soil layers are interpolated (and extrapolated) linearly. The initial profile of soil temperature and wetness is shown in Figure S2.

### 3.4 Cloud Regime Days

For the sensitivity experiments, we select a set of deep convective (Deep) days from the control simulation (P3 scheme, with a horizontal resolution of 500 m and a domain size of 200x200x27 km$^3$) and perturb the sounding or the large-scale forcing imposed. For the Deep selection, we require that the domain average of total ice presents a distinct deepening during the afternoon, characteristic of the STD convective transition. The chosen Deep days are December 17th, 21st, 23rd, and 26th. For comparison, we also select a set of shallow cumulus (ShCu) days from the control run. We identify four days with negligible ice content and minimum surface precipitation: December 9th, 13th, 27th,

and 28th. Figure S3 shows the profile of cloud liquid and total ice for our selection of cloud regime days.

## 4 Model Validation

A comparison between simulated and observed CWV, precipitation rate, LE, and H is shown in Figure 2. Results are shown for simulations using the single-moment, double-moment, and P3 microphysics schemes, in addition to the higher-resolution (P3/250m) and larger domain (P3/400km) runs.

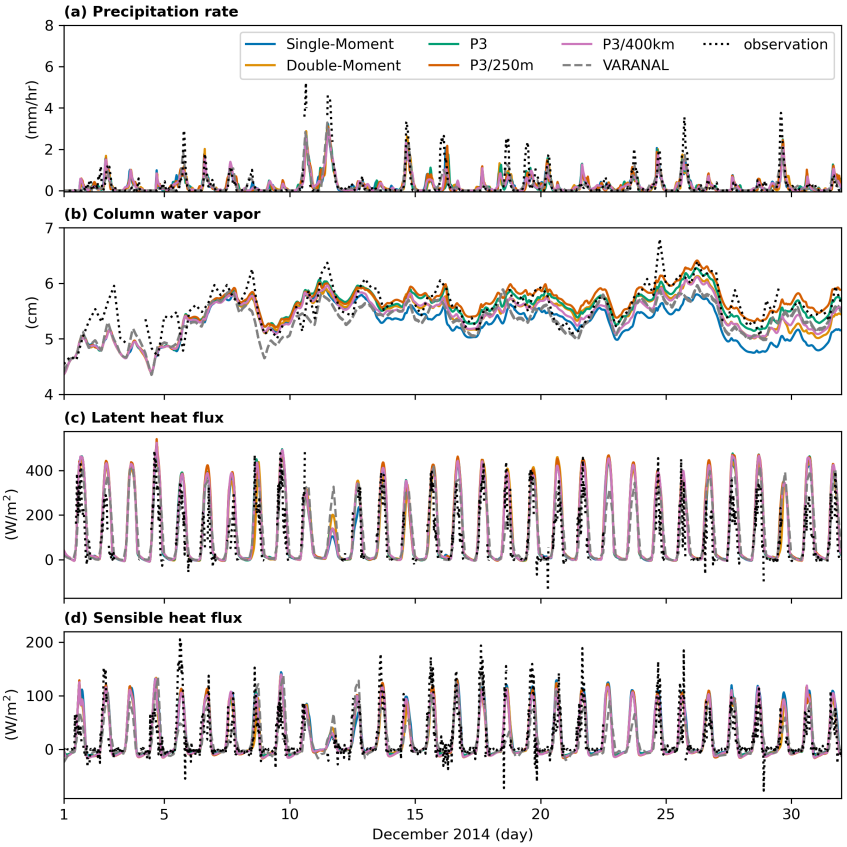


**Figure 2.** Comparison of modeling results (solid colors), large-scale forcing (dashed gray), and observations (dotted) for (a) Precipitation rate (mm/hr), (b) Column water vapor (cm), (c) Latent heat flux (W/m$^2$), and (d) Sensible heat flux (W/m$^2$) averaged over the model domain.

Simulated and observed CVW values agree very well in the first week, likely a result of the nudging imposed during the spin-up period, after which some differences begin to appear. CWV values are generally higher for the P3 scheme and lower for the single-moment run. The P3 cases exhibit the strongest correlation (Pearson) with the observations: 0.78 for P3/250m and 0.75 for both P3 and P3/400km (see the Taylor diagrams in Figure S4). Conversely, the single-moment scheme shows a weaker correlation with the observed CWV (0.56), while the double-moment scheme correlation is close to that of the P3 scheme (0.70). For the standard deviation of CWV, the model values range from 0.24 mm (P3/250m) to 0.28 mm (Single-Moment), while the observations indicate a value of 0.34 mm. Despite this difference, these statistics suggest that the model can

reproduce observed moisture content reasonably well for at least one month without resorting to any water vapor nudging.

The different simulations closely reproduce the observed surface precipitation rate, with correlations ranging from 0.76 (P3/250m) to 0.79 (P3/400km). The simulations exhibit better agreement for lower precipitation rates, while they tend to underestimate the most intense precipitation events, which are associated with MCSs. Moreover, the model precipitation did not show significant sensitivity to the microphysics, spatial resolution, or domain size. We hypothesize that the model's underestimation of intense surface precipitation could potentially be attributed to the periodic boundary conditions. These conditions might prevent the advection of MCSs that could have developed in areas outside the domain. Nevertheless, our validation results remain satisfactory, particularly considering our primary focus is locally-driven STD convective transitions.

Observed surface fluxes are reproduced reasonably well in the model runs. LE correlations with observations vary from 0.81 (double-moment) to 0.84 (P3, P3/250m, and P3/400km), while the H correlations range from 0.78 (double-moment) to 0.80 (P3, P3/250m, and P3/400km). The model only slightly overestimates the standard deviation of the observed mean LE, with the difference between model runs and observations being less than 2 W $m^{-2}$. However, it should be noted that the ECOR flux measurement system provides local measurements of surface fluxes in a grassland region (T3 site, see Figure 1b), while the model provides an average for an area of 200×200 $km^2$ (or 400×400 $km^2$ for P3/400km), entirely covered by evergreen broadleaf forest. These differences make the qualitative agreement between model simulations and observations all the more remarkable.

To evaluate the surface radiation budget, Figure 3 compares modeled and observed surface shortwave and longwave fluxes, including both downward and upward components. There is high-frequency variability in the observations that is not present in the model, likely because its values correspond to horizontal averages over the domain, whereas observational values are taken at the T3 site. Nevertheless, the model reproduces the observations satisfactorily for downward/upward surface shortwave and upward longwave fluxes (correlation ranges 0.82-0.86, Figure S5). In the case of downward longwave fluxes, the correlation is weaker, ranging from 0.57 (single and double-moment) to 0.62 (P3, P3/250m, and P3/400km), although these values are reasonable.

Overall, our simulations with different microphysics schemes compared reasonably well with the observations considered in our validation analysis. The exception was the column water vapor, where the P3 scheme showed a stronger correlation with the observations. While neither the higher resolution (P3/250m) nor the larger domain size (P3/400km) simulations demonstrated significant improvements over the P3 case, they significantly increased computational costs. This motivated our choice of the P3 scheme with 500 m horizontal resolution and a 200×200 $km^2$ domain size as the control run configuration which underlies the results presented below.

## 5 Sensitivity Experiments

To evaluate the role of moisture and vertical wind shear in the STD convective transition, a series of sensitivity experiments are carried out. First, we perturb the water vapor profile at low levels and the free troposphere to investigate the importance of low- and mid-level preconditioning. For vertical wind shear, we modify the structure of the low or upper-level jets to evaluate the relative importance of wind shear at different levels. The results in this section are associated with the mean composites for the four Deep or ShCu (section 3.4) simulated days.

Figure 4 shows the composite of cloud liquid ($r_l$), total ice ($r_i$), and rainwater ($r_r$) mixing ratios for the Deep and ShCu days averaged over the model domain. In addition

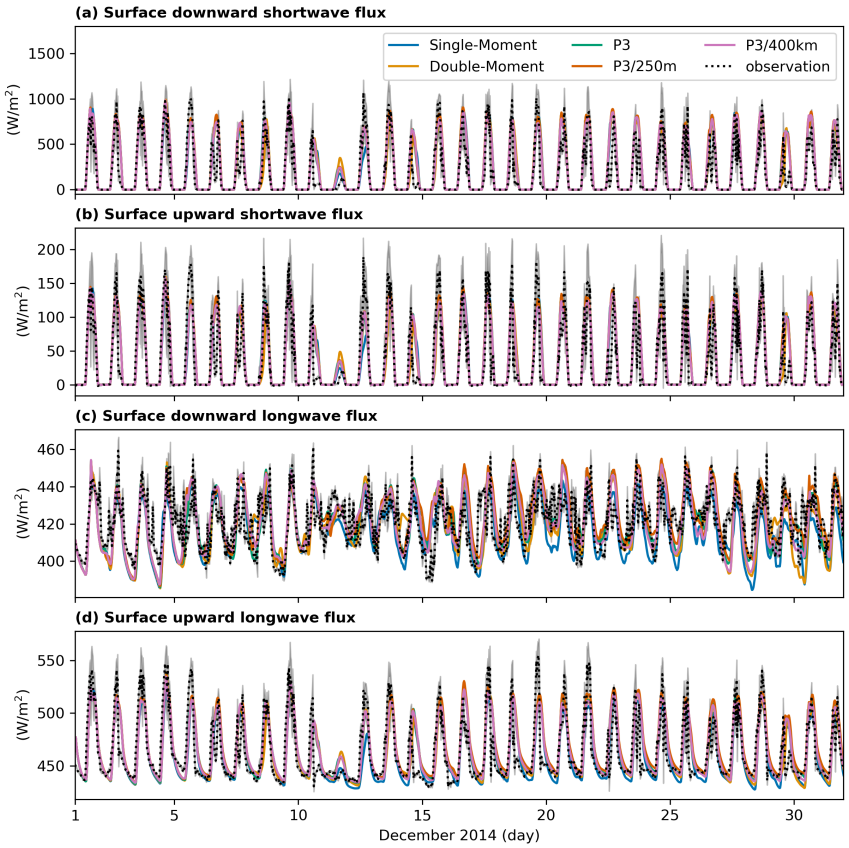


**Figure 3.** Similar to Figure 2, but for (a) downward shortwave, (b) upward shortwave, (c) downward longwave, and (d) upward longwave flux at the surface (W/m$^2$) averaged over the model domain.

to liquid water, we include the convective boundary layer (CBL) height (magenta dashed line), defined as the height at which the buoyancy flux reaches its first local minimum. The figure shows that the CBL height follows closely cloud base and the lifting condensation level, with values reaching a maximum of 1.30 km at 14:45 LST on Deep days and 1.41 km at 16:15 on ShCu days. Both regimes exhibit a peak in $r_l$ associated with shallow convection, below 3 km between 10-14 LST. Additionally, Deep days show two peaks in $r_i$. The first occurs between 12-14 LST at upper levels ($> 8$ km), associated with deep convection driven by surface heating (Martin et al., 2016; Tang et al., 2016; Zhuang et al., 2017; Tian et al., 2021). The second peak occurs a few hours later, between 16-18 LST, associated with the late afternoon STD convection transition triggered by these land-atmosphere interactions.

### 5.1 Low-Level Moisture Experiment

For the low-level moisture experiment, a moisture perturbation within the lower 1.5 km of the domain is introduced. We introduce this perturbation by multiplying the water vapor mixing ratio by a constant factor. To ensure smoothness of the vertical profile, we linearly decrease the factor to 0 between altitudes of 1.25 km and 1.75 km. For each of the Deep days selected, the model is restarted from the control run at 02 LST and the perturbation was applied. Finally, the factors are selected such that the CWV for the perturbed profile at 02 LST drops by 1, 2, 3, and 4 mm.

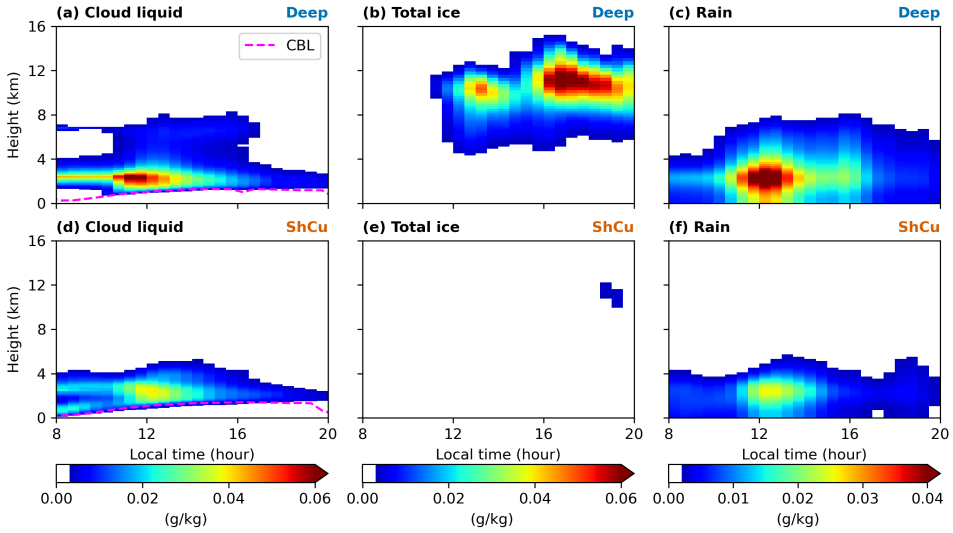


**Figure 4.** Composites for the Deep (top) and ShCu (bottom) regime days showing the diurnal cycle of domain-averaged (a,d): Cloud liquid water (colormap) and convective boundary layer (magenta dashed line), (b,e): Total ice, and (c,f): Rain content. The Deep selection includes the 17th, 21st, 23rd, and 26th of December 2014, while the ShCu selection comprises the days of the 9th, 13th, 27th, and 28th (section 3.4).

Figure 5 depicts the 30-minute average water vapor profiles at 02:15 LST, 08:15 LST, and 14:15 LST, along with the daytime CWV for both moisture sensitivity experiments (low-level and free troposphere, with the latter described in the next section). The low-level dry perturbations (continuous lines) diminish from nighttime to afternoon due to latent heat flux and moisture tendencies. Above the perturbed region, the mixing ratio values are remarkably similar, indicating minimal vertical mixing. At 14 LST, before the late afternoon STD convective transition, the lower tropospheric water vapor for the case where CWV drops by 3 mm ($BL_{3mm}$) is similar to those for the ShCu days. In terms of CWV, the experiments $BL_{3mm}$ and $BL_{4mm}$ demonstrate lower CWV values compared to ShCu days in the early morning. However, while the ShCu composite remains relatively stable throughout the diurnal cycle, the Deep composite exhibits water vapor convergence, leading to higher CWV values than the ShCu days for all experiments in the afternoon.

Figure 6 shows the magnitude (colors) and relative (contours) difference between experiments and control case for cloud liquid, total ice, and rain domain-averaged mixing ratios. In addition, the liquid water path, ice water path, and surface precipitation (lines) are also included. Cloud liquid water is reduced up to 75% near the cloud base, with a more extensive impact observed for drier scenarios from 10 to 12 LST. Above 3 km, the amount of liquid water experiences a significant increase of up to 100% during the afternoon in drier scenarios, reflecting a greater presence of warm clouds. Additionally, the peak in liquid water in drier cases occurs later, shifting from 11:45 LST in the control case to 13:15 LST for experiments $BL_{3mm}$ and $BL_{4mm}$.

Ice water content shows a significant sensitivity to low-level dry perturbations. For example, the control case exhibits an ice water path maximum of 110.1 g $m^{-2}$, declining to 67.2 g $m^{-2}$, 56.2 g $m^{-2}$, 40.0 g $m^{-2}$, and reaching a minimum of 9.5 g $m^{-2}$ with a decrease in CWV by 1, 2, 3, and 4 mm at 02 LST, respectively. The relative differences compared to the control case are 33.5%, 44.4%, 60.4%, and 90.6%, respectively, indicating a non-linear decrease in the ice water path as a function of the change in CWV.

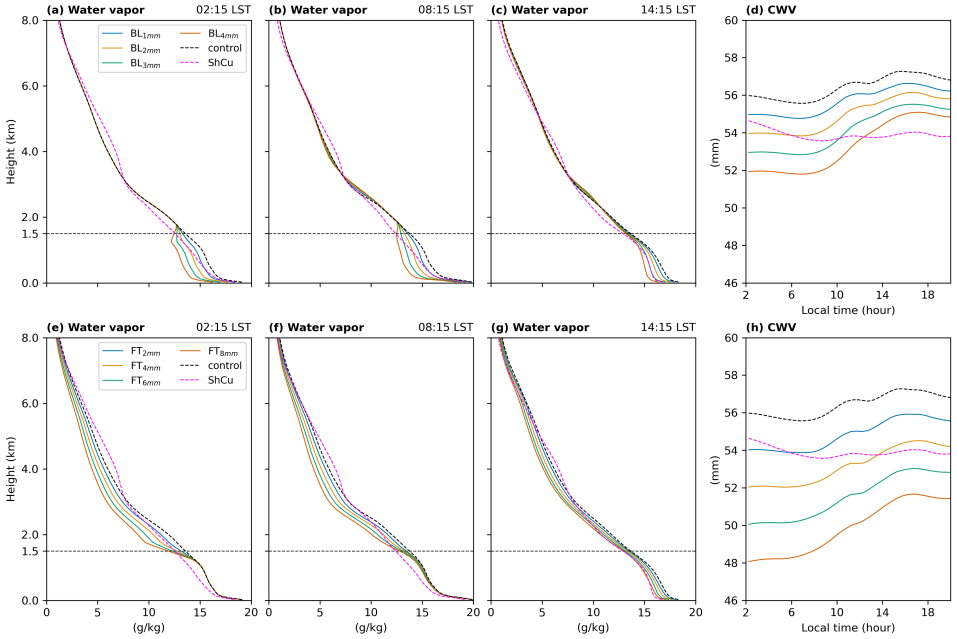


**Figure 5.** Moisture perturbation. Specific humidity (g/kg) profile at (a,e) 02:15 LST, (b,f) 08:15 LST, (c,g) 14:15 LST, and time series of (d,h) column water vapor (mm) for low-level (upper panels, solid colors) and free troposphere (lower panels, solid colors) moisture experiments. The Deep composite (control) is the dashed black line, and the ShCu composite is the dashed magenta line.

For the rain content, a decrease in drier scenarios is observed from early morning to early afternoon. While the reduction remains insignificant when reducing CWV by 1 mm, contours of 50% and 75% emerge in the drier cases. In terms of precipitation rate, the control case shows a peak of 0.86 mm $hr^{-1}$, declining to 0.78, 0.68, 0.55, and 0.42 mm $hr^{-1}$ with a decrease in CWV by 1, 2, 3, and 4 mm at 02 LST, respectively. The decrease in the maximum precipitation rate resulting from changes in CWV can be effectively modeled by a quadratic function (Figure S6). Note that despite the observed sensitivity of ice content to low-level dry perturbations, where ice content becomes negligible in the driest scenario, the model still produces significant amounts of warm precipitation for all experiments.

### 5.2 Free Troposphere Moisture Experiment

The experiments conducted in the free troposphere are analogous to the low-level moisture experiments, differing only in that the perturbation is applied above 1.5 km. We select multiplicative factors such that the CWV for the perturbed profile at 02 LST drops by 2, 4, 6, and 8 mm, respectively. These changes in CWV correspond to double what is applied in the previous section, and our choice is motivated by the weaker sensitivity of free troposphere humidity to convection, as we will show below.

The dry perturbations in the free troposphere diminish throughout the day, similarly to the low-level perturbations (Figure 5). The drier scenarios also exhibit slightly drier conditions at lower levels by early afternoon compared to the control run. The free troposphere experiments start with a lower CWV value than that of shallow days. However, the case $FT_{2mm}$ already presents higher CWV values than the shallow composite in the early morning, while $FT_{4mm}$ shows higher values than shallow days only in the

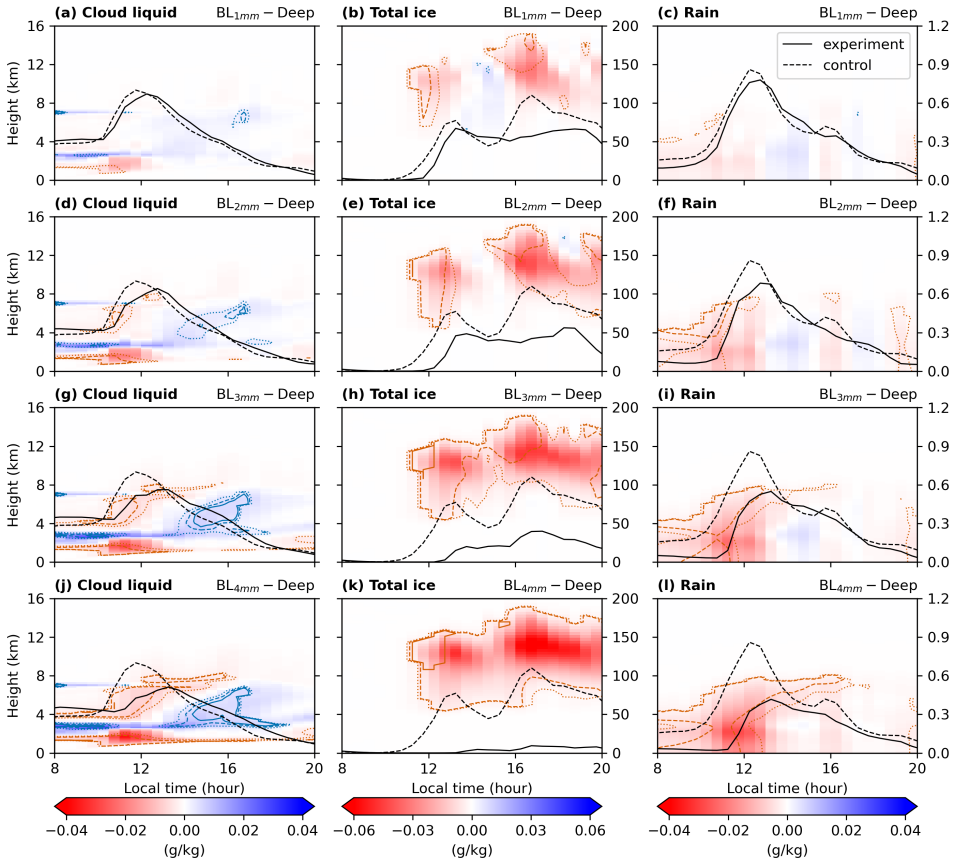


**Figure 6.** Low-level moisture experiment. The composites show the diurnal cycle of domain-averaged anomalies for (a,d,g,j) Cloud liquid water (g/kg), (b,e,h,k) Total ice (g/kg), and (c,f,i,l) Rain (g/kg) mixing ratios. Each row corresponds to a different decrease in CWV, (a-c) 1 mm, (d-f) 2 mm, (g-i) 3 mm, and (j-l) 4 mm. The colors indicate the absolute difference between each experiment and the control, while the contours show relative differences of 50% (dotted), 75% (dashed), and 100% (solid). Liquid and ice water paths (right axis, g/m$^2$) are presented along with cloud liquid and total ice, respectively, and surface precipitation rate (right axis, mm hr$^{-1}$) is shown alongside rainwater. The solid line represents the experiment, while the dashed line represents the control runs conducted during the Deep days.

afternoon (around 14 LST). For the drier cases, $FT_{6mm}$ and $FT_{8mm}$, their CWV remains lower than that of the shallow days throughout the simulation.

Figure 7 presents the results for the free-troposphere moisture experiments and control runs during the Deep days. While applying a dry perturbation above 1.5 km leads to a reduction in cloud liquid water and liquid water path throughout the troposphere, this impact is relatively minor compared to what is observed in the low-level experiments.

Cloud ice water exhibits a greater sensitivity to the free troposphere perturbations. However, the impact is still relatively minor compared to the perturbations at low levels. For instance, when the perturbation in the free troposphere and at low levels leads to a 2 mm drop in CWV, the maximum ice water path is 99.1 g m$^{-2}$ and 56.2 g m$^{-2}$, respectively. Similarly, with a 4 mm drop in CWV, the maximum ice water path is 60.9 g m$^{-2}$ and 9.5 g m$^{-2}$ for the perturbations in the free troposphere and at low levels, respectively. Moreover, the driest free troposphere case ($FT_{8mm}$) still exhibits significant

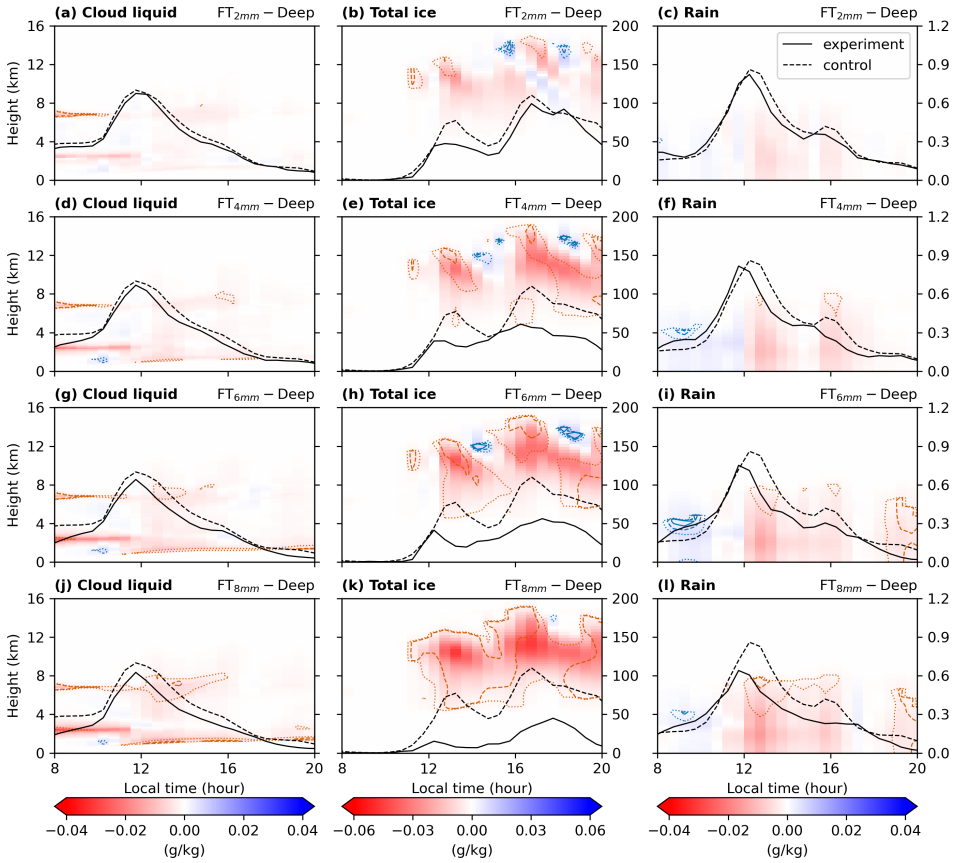


**Figure 7.** Same as Figure 6, but for the free troposphere moisture experiment instead, where the decreases in CWV were 2, 4, 6, and 8 mm.

ice water path values, with a maximum of 45.0 g $m^{-2}$ at 17:45 LST, being even greater than the value observed for the experiment where CWV is reduced by 3 mm at low levels ($BL_{3mm}$, 40.0 g $m^{-2}$).

Rain content also shows a reasonable sensitivity to the free troposphere perturbations, although it is minor compared to low-level perturbations. For example, when the perturbation in the free troposphere and at low levels leads to a 2 mm drop in CWV, the peak of precipitation is 0.82 mm $hr^{-1}$ and 0.68 mm $hr^{-1}$, respectively. Similarly, with a 4 mm drop in CWV, the peak for the free troposphere experiment remains the same (0.82 mm $hr^{-1}$) while the low-level perturbation shows 0.42 mm $hr^{-1}$. Finally, the driest free troposphere case ($FT_{8mm}$) shows a maximum of 0.64 mm $hr^{-1}$, which better relates with experiment $BL_{2mm}$ (0.68 mm $hr^{-1}$).

### 5.3 Wind Jet Experiment

To assess the impact of wind shear on the deepening of convective clouds in the Amazon, we perform sensitivity experiments in which the low- or high-level jets are modified. Each jet's intensity, amplitude, and altitude are changed separately. The modified wind profiles are used to force the model, with nudging applied with a timescale of 2 hours throughout the simulation.

In order to have better control of the shape of the wind profiles and easily generate sensitivity tests, we approximate the imposed wind using an analytical formula. More

specifically, considering the shape of the wind speed, we model this quantity as the superposition of two Gaussian functions, each representing a jet. The average wind speed is fitted to this function, and the fitting parameters are given in Table S1. The wind direction was fitted to a piece-wise linear function. (Figure 8b). The wind direction is constant in the bottom ∼2 km. It veers clockwise at a constant rate of about 14° km$^{-1}$ from 2 to 15 km, and counterclockwise at a rate of -28° km$^{-1}$ from 15 to 20 km, and it is constant above 20 km (not shown). The wind speed and direction imposed for control runs are shown in Figure 8a-b (solid black line).

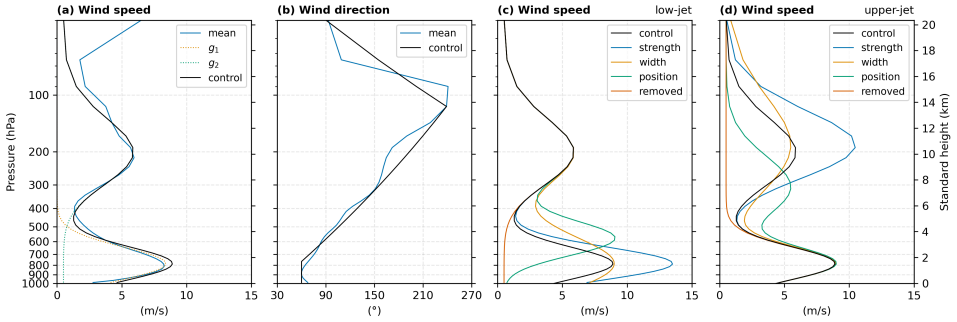


**Figure 8.** Wind profiles for the jet experiments control run showing: (a) large-scale wind speed and (b) wind direction, as measured (blue) and as idealized (black). Sensitivity experiments perturbed the wind speed profile of either the (c) low-level or (d) upper-level wind jets by intensifying (blue), widening (orange), shifting (green), or removing the jet (red).

For each jet, we conduct 4 experiments in which we (1) increase the jet strength, (2) increase the width, (3) shift the peak position, and (4) remove the jet entirely while keeping the wind direction constant in all cases. The modified wind profiles are shown in Figures 8c-d. For each experiment, the model is restarted from the control run at 02 LST of each one of the four Deep days selected, and the modified wind profiles are applied to force the model with a 2-h nudging timescale.

Figure 9 presents the results for the low-level jet experiments. While the jet position significantly affects cloud liquid water, the jet width has a negligible impact. The higher position possibly enhances the low-level updrafts, leading to an increase of $r_l$ above 2 km, particularly in the late afternoon (around 16 LST), where $r_l$ can increase by as much as 100%. Removing the low-level jet also exhibits a similar impact on cloud liquid water, although the anomalies are smaller than those associated with the higher jet. The stronger jet only slightly impacts the cloud liquid water. Although the jet influences the cloud water profile, the integrated liquid water path is similar in all experiments and does not significantly differ from the control.

The cloud ice content is more significantly affected by the low-level jet. The control experiment exhibits peaks in ice water path at 12:45 LST and 16:15 LST. The stronger jet simulation shows positive anomalies before 12 LST and after 16 LST, resulting in an increase in $r_i$ of up to 100%, with negative anomalies observed in between. For the wider jet, a positive anomaly dominates throughout the diurnal cycle, especially between 12-17 LST, when $r_i$ increases up to 100% above 12 km. However, there is only a modest increment in ice water path. The higher jet shows a decrease ranging from 50-75% in $r_i$ around 12 LST and an increase afterwards. There is a delay of the convective activity, with a suppression at 12 LST and an increase around 16 LST. When the low-level jet is removed, the ice water path is substantially reduced, both at 12 and 16 LST (up to 75%), with the maximum being reached only around 17:45.

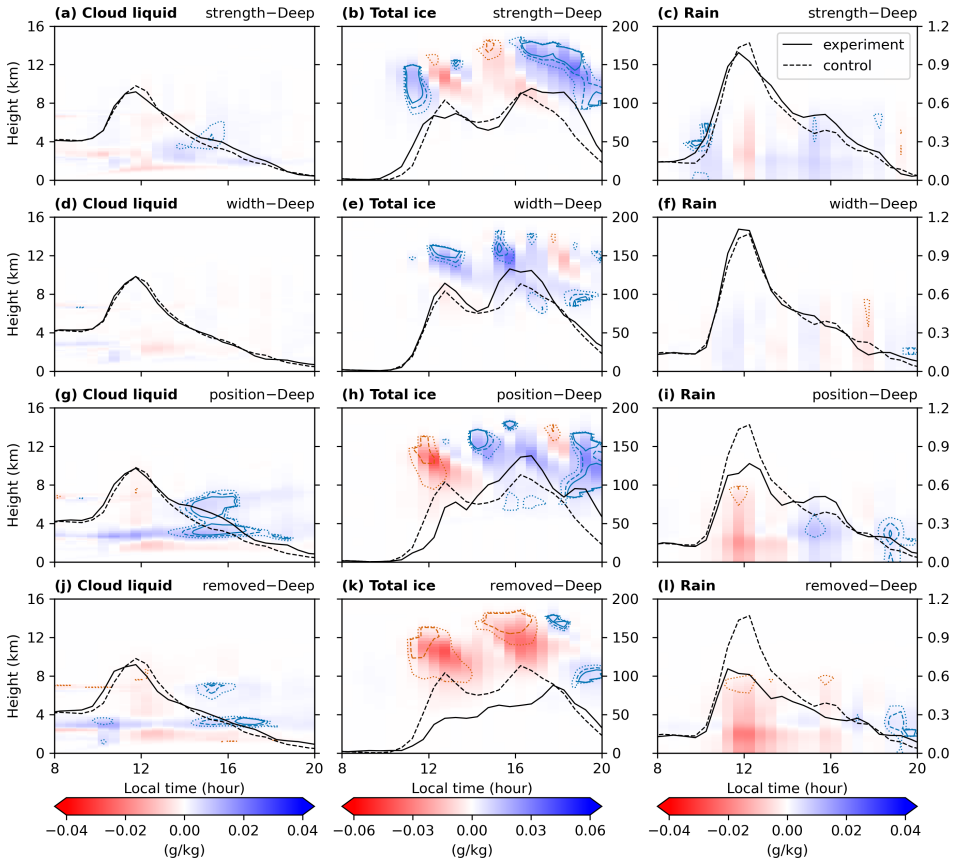


**Figure 9.** Low-level jet experiment. The composites show the diurnal cycle of domain-averaged anomalies for (a,d,g,j) Cloud liquid water (g/kg), (b,e,h,k) Total ice (g/kg), and (c,f,i,l) Rain (g/kg) mixing ratios. Each row corresponds to a different low-level jet perturbation, (a-c) strength, (d-f) width, (g-i) position, and (j-l) removed entirely. The colors indicate the absolute difference between each experiment and the control, while the contours show relative differences of 50% (dotted), 75% (dashed), and 100% (solid). Liquid and ice water paths (right axis, g/m$^2$) are presented along with cloud liquid and total ice, respectively, and surface precipitation rate (right axis, mm hr$^{-1}$) is shown alongside rainwater. The solid line represents the experiment, while the dashed line represents the control runs conducted during the Deep days.

Rain content follows the changes in total ice mixing ratio, with negative (positive) anomalies where ice decreases (increases). However, changes in $r_r$ are less significant, with smaller areas showing changes greater than 50%. While the surface precipitation shows minimal impact in the stronger and wider jet experiments, it exhibits notable differences for the other two cases. For the higher jet, precipitation decreases around noon and increases in the late afternoon, following the changes in ice water path. In the absence of a jet, precipitation is particularly reduced between 12-15 LST, with the noon peak being roughly 40% lower than that observed in the control runs.

Figure 10 presents the results for the upper-level jet experiments. There is a striking contrast with the low-level jet results. The upper-level jet affects convection only in the upper troposphere, with negligible impacts on liquid water. Overall, the experiments show an alternating increasing and decreasing ice content pattern. This is related to a delay in convection, which can be more easily noticed on the ice water path curves. Both

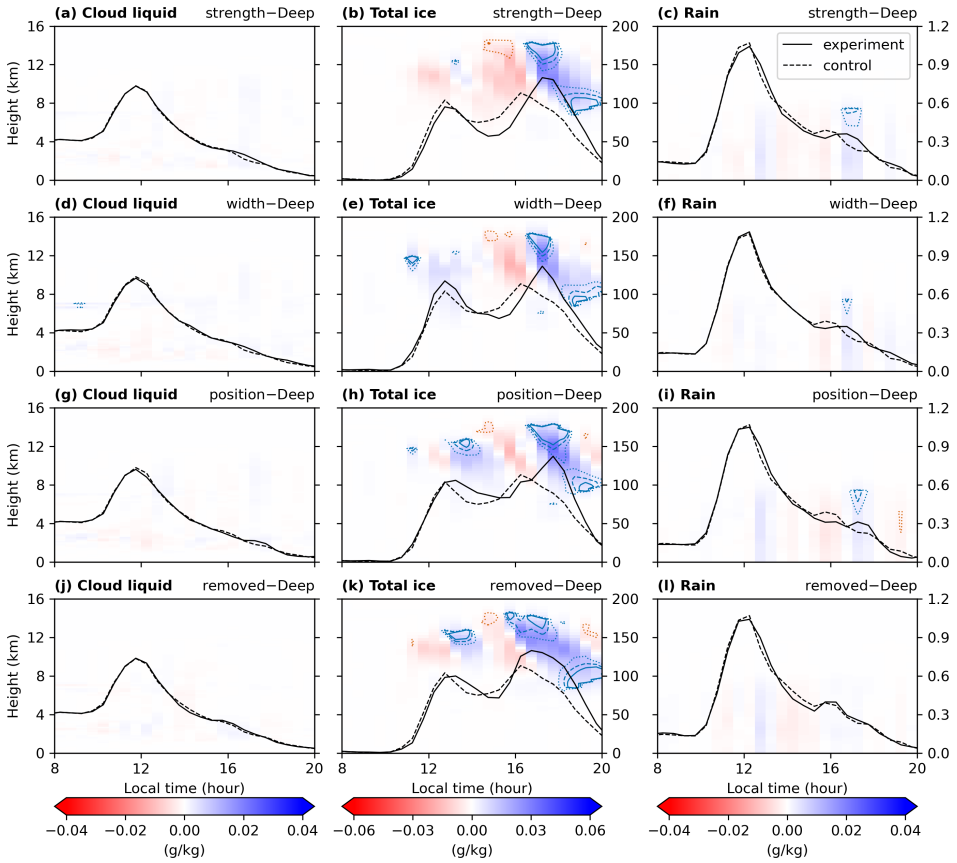


**Figure 10.** Same as Figure 9, but for the upper-level jet experiment instead.

the noon and afternoon peaks are displaced to later times, and the afternoon peak also gets more intense. The exception is the wider jet experiment, where the noon peak slightly increases and is not delayed. The changes are more significant after 17 LST when all experiments exhibit an increase of up to 100% in ice water. In the case of the removed jet, the afternoon peak occurs 30 minutes later (16:45 LST). For the stronger and wider jet experiments, the peak is delayed by 1 hour (17:15 LST), and for the jet with a relatively lower position, the peak occurs 1.5 hours later (17:45 LST). Nonetheless, there is no significant change in the rain content and surface precipitation.

## 6 Discussion

While several studies in the literature have employed CRMs to simulate convective properties in both continental (M. F. Khairoutdinov & Randall, 2003; M. Khairoutdinov & Randall, 2006; Henderson & Pincus, 2009; Cecchini et al., 2022) and ocean (Blossey et al., 2007; M. F. Khairoutdinov et al., 2009; Liu et al., 2015; Blossey et al., 2021) regions, we conduct simulations specifically for the central Amazon by coupling a CRM with a LSM, thus explicitly representing biosphere-atmosphere feedbacks, which plays a crucial role on convection over the Amazon tropical forest (Silva Dias et al., 2002). Vilà-Guerau de Arellano et al. (2020) utilized a large-eddy model combined with a different LSM to investigate the diurnal cycle of energy, moisture, and carbon dioxide from clear to cloudy conditions. Nevertheless, their study relied only upon a specific day during the Amazon dry season and did not address deep convection. Although the recent work by Gonçalves et al. (2022) also utilized a CRM coupled with an LSM to simulate convec-

tion in the central Amazon, they did not evaluate the evolution of moisture content and surface latent and sensible heat fluxes. This restricts the validation of their simulations in reproducing these crucial convective properties, which we have addressed in our study. Specifically, we evaluate the model performance using single-moment, double-moment, and P3 microphysics schemes. Only the CWV exhibits a noticeable sensitivity to the microphysics, where the P3 scheme shows the strongest correlation (Pearson, 0.8) with observations. Varying the horizontal resolution (from 500 to 250 m) and domain size (from $200\times200\times27$ to $400\times400\times27$ km$^3$) reveals minimal sensitivity to the model results. For the surface fluxes, the P3 microphysics scheme indicates a correlation of about 0.8 for both latent heat and sensible heat fluxes. Overall, our results demonstrate that our simulations satisfactorily reproduce the convective properties in the central Amazon.

Our sensitivity experiments indicate that the humidity in the early morning at lower levels plays a crucial role in the late afternoon STD convective transition in the Amazon. By reducing water vapor in the lowest 1.5 km, the diurnal peak of the ice water path substantially drops with changes in CWV, whereas a change of 2 mm causes a reduction of ice in the range of 50-75%, and a change of 4 mm results in negligible ice during the simulation. Moreover, the maximum precipitation rate demonstrates an approximately quadratic decrease with variations in the low-level CWV. Schiro et al. (2016) examined the relationship between precipitation and CWV by calculating the conditionally averaged precipitation to CWV using local observations of both variables at corresponding times. They observed that the probability and intensity of precipitation can be roughly characterized by an exponential function of CWV magnitude. It is essential to highlight that our approach differs from that of Schiro et al. (2016). We used the domain-average for maximum afternoon precipitation, while CWV precedes the diurnal cycle. This procedural difference somewhat justifies why we observed a quadratic relationship instead of an exponential one, as there is no contradiction between these results. Furthermore, our findings indicated that achieving a comparable reduction in ice water path or precipitation, as observed in the low-level experiments, requires reducing the column water vapor by a factor of two or more in the free troposphere.

While M. Khairoutdinov and Randall (2006) conducted experiments that differed from those designed in this study and were limited to a single idealized case during TRMM-LBA on February 23, 1999, they similarly indicated that free troposphere preconditioning plays a minor role in convection in the Amazon. Based on GoAmazon2014/5 observations, Ghate and Kollias (2016) noted that locally-driven precipitating days during the dry season show an early morning water vapor excess above the boundary layer while Zhuang et al. (2017); Tian et al. (2021) found that deep convective days exhibit a moister environment extending from the surface to higher levels, regardless of the season. Schiro and Neelin (2019) showed that the onset and probability of the STD transition are closely linked to both lower-free-tropospheric moisture (700–900 hPa) and boundary layer moisture. Conversely, MSC likelihood rises with higher lower-free-tropospheric humidity, while the relationship with boundary layer moisture is less distinct. The relative importance of moisture to convection can also vary based on the regions being studied. Focusing on the Tropical Western Pacific region on Nauru Island, Holloway and Neelin (2009) found a strong correlation between observed precipitation and moisture variability in the free troposphere, with limited variability in the boundary layer. Additionally, Bretherton et al. (2004) also highlighted the importance of free-tropospheric humidity to convection over the Tropical Oceans.

Vertical wind shear primarily impacts the peak timing of ice water in our simulations. Furthermore, our findings indicate that convection is enhanced during the afternoon when the low-level wind is idealized using a jet of larger width, moderate strength, and with a relatively higher peak position from around 2 to 4 km. Conversely, the upper-level wind has a minor influence on convective intensity. M. Khairoutdinov and Randall (2006) designed experiments employing an idealized large-scale wind forcing and a free

wind shear environment. Similar to our results, the STD transition was not prevented by removing vertical wind shear. Cecchini et al. (2022) also conducted numerical experiments to quantify the impact of vertical wind shear in the central Amazon, specifically targeting shallow cumulus convection during a typical day in the dry season. By introducing incremental changes in the large-scale wind speed across the entire vertical domain, the authors observed a weakening of convective intensity, suggesting that vertical wind shear prevents the STD convective transition. Here, we have identified that the vertical level of wind shear significantly influences its impact on convection. Moreover, while stronger vertical wind shear suppresses the initial phase of convection, the STD convective transition still occurs, albeit with a delay ranging from a few minutes to an hour.

In contrast to prior observational studies, our modeling results offer quantitative insights into the role of vertical wind shear in Amazonian convection. For example, Zhuang et al. (2017) observed that ShCu days are linked to stronger mid-level wind shear during the wet season. We observe that when the upper-level jet is shifted from around 12 to 8 km, which is related to mid-level wind shear, the trigger for the STD transition is only delayed by about 1.5 hours. While Chakraborty et al. (2018) indicated that more intense low-level shear is associated with shallow convection during the transition season, we observe that stronger low-level shear has little influence on cloud liquid water and might only provoke a delay in the late afternoon STD transition.

Thus, our findings suggest that a moderate shear environment might more efficiently separate downdrafts and updrafts within the cloud while concurrently organizing the convergence of low-level water vapor within the cloud layers. A wider jet leads to a smoother and more gradual shift in wind shear, extending from the surface to higher altitudes, thereby also organizing the water vapor convergence from below the cloud base to higher levels. Given the dependence of water vapor convergence on low-level humidity, convection demonstrates heightened sensitivity to boundary layer humidity. Meanwhile, the upper-level jet primarily impacts the extensive cloud anvil, exerting a relatively minor influence on ice content above 8 km. Finally, these results collectively suggest that dynamic factors may exert a more pronounced influence on convection in the Amazon.

## 7 Conclusions

While numerous observational studies have explored the environmental controls on convection in the Amazon (Itterly et al., 2016; Ghate & Kollias, 2016; Zhuang et al., 2017; Schiro et al., 2016, 2018; Chakraborty et al., 2018; Tian et al., 2021; Giangrande et al., 2023), we have specifically addressed this problem through high-resolution idealized simulations. We employ the System for Atmospheric Modeling (SAM) model coupled with a LSM to perform simulations for the Amazon region in December 2014. The model is forced with the large-scale fields from the variational analysis, and the observations from the GoAmazon2014/5 experiment are used to validate the model results. The LSM default input parameters are modified according to in-situ and satellite observations over the Amazon region, and fine-tuning tests focused on improving the model agreement with the observations. The simulations consistently reproduce the observations for precipitation, column water vapor (CWV), surface latent and sensible heat fluxes, and surface radiation fluxes. Sensitivity tests demonstrate that simulations conducted using a single-moment microphysics scheme drifted towards a drier state, while simulations with the P3 microphysics scheme more closely reproduce the observed water budget. For a more detailed validation of the LSM, having more comprehensive observations of the soil properties (e.g., temperature and wetness down to 4 m) would be necessary.

In light of recent observational studies addressing the shallow-to-deep (STD) convective transition (Ghate & Kollias, 2016; Zhuang et al., 2017; Tian et al., 2021), our study has the advantage of conducting idealized sensitivity experiments in which only one en-

vironmental control—moisture or vertical wind shear at low or high levels—is modified at a time. This approach efficiently isolates their influence in controlling convection. The pre-convective humidity at low levels had the greatest impact on convection. The diurnal peak in the ice water path robustly decays with changes in CWV within the lower 1.5 km. To have a comparable impact on the diurnal cycle of convection, it is necessary to reduce free tropospheric CWV by approximately twice the amount in the lower levels. Vertical wind shear mainly affects the ice water peak timing. A wider low-level jet of moderate strength possibly facilitates the STD convective transition by organizing low-level water vapor convergence and potentially separating downdrafts and updrafts within the cloud. The upper-level wind shear has a minor influence over convection in the Amazon.

While our results provide quantitative information on the role of moisture and wind shear in convection, we suggest that sensitivity experiments be conducted using different cloud-resolving models. For instance, SAM uses periodic lateral conditions, artificially impacting the numerical results. Using multiple models can aid in evaluating the robustness of the findings and identifying potential model biases. Although our sensitivity experiments identified that the maximum afternoon precipitation rate decreases roughly quadratically with changes in pre-convective CWV, particularly in the low-level experiment, it is important to note that this relationship was derived from only four values of moisture perturbation. This limitation restricts the significance of the findings. The robustness of this conclusion should be further addressed, with a particular focus on understanding the associated mechanism for this relationship. Finally, we also recommend that future studies conduct specific experiments to investigate the role of water vapor convergence and the effects of large-scale wind direction on deep convection.

## 8 Data Availability

The GoAmazon2014/5 observations are publicly available at `https://www.arm.gov/research/campaigns/amf2014goamazon`. The large-scale forcing data based on the variational analysis for the GoAmazon2014/5 experiment is available at the ARM Archive: `http://iop.archive.arm.gov/arm-iop/0eval-data/xie/scm-forcing/iop_at_mao/`. The Moderate Resolution Imaging Spectroradiometer (MODIS) data for land cover and leaf area index can be downloaded through the Application for Extracting and Exploring Analysis Ready Samples ($A\rho\rho$EEARS, `https://appeears.earthdatacloud.nasa.gov/`). The Global Land Data Assimilation System (GLDAS) data for soil temperature and soil wetness are available at `https://disc.gsfc.nasa.gov/datasets/GLDAS_NOAH025_3H_2.1/summary`. For further assistance concerning the model input files and the necessary modifications in the SAM's source code to perform the moisture perturbations as described in section 5.1 and section 5.2, please refer to the author.

**Acknowledgments**

The authors express their gratitude to Marat Khairoutdinov for providing access to the SAM code and for offering valuable assistance with the Land Surface Model. The technical support and advanced computing resources from University of Hawai'i Information Technology Services – Cyberinfrastructure, funded in part by the National Science Foundation CC* awards # 2201428 and # 2232862 are gratefully acknowledged. We also acknowledge the data from the Atmospheric Radiation Measurement (ARM) Program sponsored by the U.S. Department of Energy, Office of Science, Office of Biological and Environmental Research, Climate and Environmental Sciences Division. L.A.M.V. acknowledges the Brazilian National Council for Scientific and Technological Development (CNPq) graduate fellowship (grant number 148652/2019-0). Additionally, gratitude is extended to the Coordination for the Improvement of Higher Education Personnel (CAPES) fellowship (grant number 88887.571091/2020-00). H.M.J.B acknowledges support from the

U.S. Department of Energy, Office of Science, Biological and Environmental Research program under Award Number DE-SC-0023058.

## References

Adams, D. K., Barbosa, H. M. J., & Gaitán De Los Ríos, K. P. (2017). A spatiotemporal water vapor–deep convection correlation metric derived from the amazon dense gnss meteorological network. *Monthly Weather Review*, *145*(1), 279–288. doi: 10.1175/MWR-D-16-0140.1

Adams, D. K., Fernandes, R. M. S., Holub, K. L., Gutman, S. I., Barbosa, H. M. J., Machado, L. A. T., ... Tanaka, L. M. S. (2015). The amazon dense GNSS meteorological network: A new approach for examining water vapor and deep convection interactions in the tropics. *Bulletin of the American Meteorological Society*, *96*(12), 2151-2165. doi: 10.1175/BAMS-D-13-00171.1

Adams, D. K., Gutman, S. I., Holub, K. L., & Pereira, D. S. (2013). Gnss observations of deep convective time scales in the amazon. *Geophysical Research Letters*, *40*(11), 2818-2823. doi: 10.1002/grl.50573

ARM, Atmospheric Radiation Measurement. (2013). *Data quality assessment for ARM radiation data (QCRAD1LONG). 2013-12-20 to 2015-12-01, ARM mobile facility (mao) manacapuru, amazonas, brazil; amf1 (m1).* Compiled by D. Zhang, Atmospheric Radiation Measurement (ARM) Archive, Oak Ridge, Tennessee, USA. Retrieved from `http://dx.doi.org/10.5439/1227214`

ARM, Atmospheric Radiation Measurement. (2014a). *Balloon-borne sounding system (SONDEWNPN). 2014-01-01 to 2015-12-01, ARM mobile facility (mao) manacapuru, amazonas, brazil; amf1 (m1).* Compiled by: Keeler, E., and Burk, K., Atmospheric Radiation Measurement (ARM) Archive, Oak Ridge, Tennessee, USA. Retrieved from `https://doi.org/10.5439/1595321`

ARM, Atmospheric Radiation Measurement. (2014b). *Quality controlled eddy correlation flux measurement (30QCECOR). 2014-04-03 to 2015-12-01, ARM mobile facility (mao) manacapuru, amazonas, brazil; amf1 (m1).* Compiled by S. Xie, Atmospheric Radiation Measurement (ARM) Archive, Oak Ridge, Tennessee, USA. Retrieved from `http://dx.doi.org/10.5439/1097546`

Bechtold, P., Chaboureau, J.-P., Beljaars, A., Betts, A. K., Köhler, M., Miller, M., & Redelsperger, J.-L. (2004). The simulation of the diurnal cycle of convective precipitation over land in a global model. *Quarterly Journal of the Royal Meteorological Society*, *130*(604), 3119-3137. doi: 10.1256/qj.03.103

Betts, A. K. (2002). Evaluation of the diurnal cycle of precipitation, surface thermodynamics, and surface fluxes in the ECMWF model using LBA data. *Journal of Geophysical Research*, *107*(D20). doi: 10.1029/2001jd000427

Betts, A. K., & Jakob, C. (2002). Study of diurnal cycle of convective precipitation over amazonia using a single column model. *Journal of Geophysical Research: Atmospheres*, *107*(D23), ACL 25–1–ACL 25–13. doi: 10.1029/2002jd002264

Blossey, P. N., Bretherton, C. S., Cetrone, J., & Kharoutdinov, M. (2007). Cloud-resolving model simulations of KWAJEX: Model sensitivities and comparisons with satellite and radar observations. *J. Atmos. Sci.*, *64*(5), 1488–1508.

Blossey, P. N., Bretherton, C. S., & Mohrmann, J. (2021). Simulating observed cloud transitions in the northeast pacific during CSET. *Monthly Weather Review*. doi: 10.1175/mwr-d-20-0328.1

Bretherton, C. S., Peters, M. E., & Back, L. E. (2004). Relationships between water vapor path and precipitation over the tropical oceans. *Journal of Climate*, *17*(7), 1517 - 1528. doi: 10.1175/1520-0442(2004)017⟨1517:RBWVPA⟩2.0.CO;2

Cecchini, M. A., de Bruine, M., Vilà-Guerau de Arellano, J., & Artaxo, P. (2022). Quantifying vertical wind shear effects in shallow cumulus clouds over amazonia. *Atmospheric Chemistry and Physics*, *22*(17), 11867–11888. doi:

10.5194/acp-22-11867-2022

Chakraborty, S., Schiro, K. A., Fu, R., & Neelin, J. D. (2018). On the role of aerosols, humidity, and vertical wind shear in the transition of shallow-to-deep convection at the green ocean amazon 2014/5 site. *Atmospheric Chemistry and Physics*, *18*(15), 11135–11148. doi: 10.5194/acp-18-11135-2018

Collier, J. C., & Bowman, K. P. (2004). Diurnal cycle of tropical precipitation in a general circulation model. *Journal of Geophysical Research*, *109*(D17). doi: 10.1029/2004jd004818

Collins, W. D., Rasch, P. J., Boville, B. A., Hack, J. J., McCaa, J. R., Williamson, D. L., ... Zhang, M. (2006). The formulation and atmospheric simulation of the community atmosphere model version 3 (CAM3). *Journal of Climate*, *19*(11), 2144–2161. doi: 10.1175/jcli3760.1

Dai, A., & Trenberth, K. E. (2004). The diurnal cycle and its depiction in the community climate system model. *Journal of Climate*, *17*(5), 930–951. doi: 10.1175/1520-0442(2004)017⟨0930:tdcaid⟩2.0.co;2

Dee, D. P., Uppala, S. M., Simmons, A. J., Berrisford, P., Poli, P., Kobayashi, S., ... Vitart, F. (2011). The ERA-interim reanalysis: configuration and performance of the data assimilation system. *Quarterly Journal of the Royal Meteorological Society*, *137*(656), 553–597. doi: 10.1002/qj.828

Derbyshire, S. H., Beau, I., Bechtold, P., Grandpeix, J.-Y., Piriou, J.-M., Redelsperger, J.-L., & Soares, P. M. M. (2004). Sensitivity of moist convection to environmental humidity. *Quarterly Journal of the Royal Meteorological Society*, *130*(604), 3055-3079. doi: 10.1256/qj.03.130

Freitas, S. R., Grell, G. A., Chovert, A. D., Silva Dias, M. A. F., & de Lima Nascimento, E. (2024). A parameterization for cloud organization and propagation by evaporation-driven cold pool edges. *Journal of Advances in Modeling Earth Systems*, *16*(1), e2023MS003982. doi: 10.1029/2023MS003982

Freitas, S. R., Putman, W. M., Arnold, N. P., Adams, D. K., & Grell, G. A. (2020). Cascading toward a kilometer-scale GCM: Impacts of a scale-aware convection parameterization in the goddard earth observing system GCM. *Geophysical Research Letters*, *47*(17). doi: 10.1029/2020gl087682

Friedl, M. A., Sulla-Menashe, D., Tan, B., Schneider, A., Ramankutty, N., Sibley, A., & Huang, X. (2010). Modis collection 5 global land cover: Algorithm refinements and characterization of new datasets. *Remote Sensing of Environment*, *114*(1), 168-182. doi: 10.1016/j.rse.2009.08.016

Ghate, V. P., & Kollias, P. (2016). On the controls of daytime precipitation in the amazonian dry season. *Journal of Hydrometeorology*, *17*(12), 3079–3097. doi: 10.1175/jhm-d-16-0101.1

Giangrande, S. E., Biscaro, T. S., & Peters, J. M. (2023). Seasonal controls on isolated convective storm drafts, precipitation intensity, and life cycle as observed during goamazon2014/5. *Atmospheric Chemistry and Physics*, *23*(9), 5297–5316. doi: 10.5194/acp-23-5297-2023

Gonçalves, L. J. M., Coelho, S. M. S. C., Kubota, P. Y., & Souza, D. C. (2022). Interaction between cloud–radiation, atmospheric dynamics and thermodynamics based on observational data from goamazon 2014/15 and a cloud-resolving model. *Atmospheric Chemistry and Physics*, *22*(23), 15509–15526. doi: 10.5194/acp-22-15509-2022

Grabowski, W. W., Bechtold, P., Cheng, A., Forbes, R., Halliwell, C., Khairoutdinov, M., ... Xu, K.-M. (2006). Daytime convective development over land: A model intercomparison based on LBA observations. *Quarterly Journal of the Royal Meteorological Society*, *132*(615), 317–344. doi: 10.1256/qj.04.147

Gupta, A. K., Deshmukh, A., Waman, D., Patade, S., Jadav, A., Phillips, V. T. J., ... Gonçalves, F. L. T. (2023). The microphysics of the warm-rain and ice crystal processes of precipitation in simulated continental convective storms. *Communications Earth & Environment*, *4*(1). doi: 10.1038/

s43247-023-00884-5

Henderson, P. W., & Pincus, R. (2009). Multiyear evaluations of a cloud model using ARM data. *J. Atmos. Sci.*, *66*(9), 2925–2936.

Henkes, A., Fisch, G., Machado, L. A. T., & Chaboureau, J.-P. (2021). Morning boundary layer conditions for shallow to deep convective cloud evolution during the dry season in the central amazon. *Atmospheric Chemistry and Physics*, *21*(17), 13207–13225. doi: 10.5194/acp-21-13207-2021

Hohenegger, C., & Stevens, B. (2013). Preconditioning deep convection with cumulus congestus. *Journal of the Atmospheric Sciences*, *70*(2), 448–464. doi: 10.1175/jas-d-12-089.1

Holloway, C. E., & Neelin, J. D. (2009). Moisture vertical structure, column water vapor, and tropical deep convection. *Journal of the Atmospheric Sciences*, *66*(6), 1665 - 1683. doi: 10.1175/2008JAS2806.1

Houze Jr, R. A. (2004). Mesoscale convective systems. *Reviews of Geophysics*, *42*(4). doi: 10.1029/2004RG000150

Itterly, K. F., Taylor, P. C., & Dodson, J. B. (2018). Sensitivity of the amazonian convective diurnal cycle to its environment in observations and reanalysis. *Journal of Geophysical Research: Atmospheres*, *123*(22). doi: 10.1029/2018jd029251

Itterly, K. F., Taylor, P. C., Dodson, J. B., & Tawfik, A. B. (2016). On the sensitivity of the diurnal cycle in the amazon to convective intensity. *Journal of Geophysical Research: Atmospheres*, *121*(14), 8186–8208. doi: 10.1002/2016jd025039

Jewtoukoff, V., Plougonven, R., & Hertzog, A. (2013). Gravity waves generated by deep tropical convection: Estimates from balloon observations and mesoscale simulations. *Journal of Geophysical Research: Atmospheres*, *118*(17), 9690-9707. doi: 10.1002/jgrd.50781

Khairoutdinov, M., & Randall, D. (2006). High-resolution simulation of shallow-to-deep convection transition over land. *Journal of the Atmospheric Sciences*, *63*(12), 3421–3436. doi: 10.1175/jas3810.1

Khairoutdinov, M. F., Krueger, S. K., Moeng, C.-H., Bogenschutz, P. A., & Randall, D. A. (2009). Large-eddy simulation of maritime deep tropical convection. *Journal of Advances in Modeling Earth Systems*, *2*. doi: 10.3894/james.2009.1.15

Khairoutdinov, M. F., & Randall, D. A. (2003). Cloud resolving modeling of the ARM summer 1997 iop: Model formulation, results, uncertainties, and sensitivities. *Journal of the Atmospheric Sciences*, *60*(4), 607 - 625. doi: 10.1175/1520-0469(2003)060⟨0607:CRMOTA⟩2.0.CO;2

Lee, J. M., & Khairoutdinov, M. (2015). A simplified land model (SLM) for use in cloud-resolving models: Formulation and evaluation. *Journal of Advances in Modeling Earth Systems*, *7*(3), 1368–1392. doi: 10.1002/2014ms000419

Lin, X., Randall, D. A., & Fowler, L. D. (2000, 12). Diurnal variability of the hydrologic cycle and radiative fluxes: Comparisons between observations and a GCM. *Journal of Climate*, *13*(23), 4159–4179. doi: 10.1175/1520-0442(2000)013⟨4159:dvothc⟩2.0.co;2

Liu, Z., Muhlbauer, A., & Ackerman, T. (2015). Evaluation of high-level clouds in cloud resolving model simulations with ARM and KWAJEX observations. *J. Adv. Model. Earth Syst.*, *7*(4), 1716–1740.

Maher, P., Vallis, G. K., Sherwood, S. C., Webb, M. J., & Sansom, P. G. (2018). The impact of parameterized convection on climatological precipitation in atmospheric global climate models. *Geophysical Research Letters*, *45*(8), 3728–3736. doi: 10.1002/2017gl076826

Mapes, B., Milliff, R., & Morzel, J. (2009). Composite life cycle of maritime tropical mesoscale convective systems in scatterometer and microwave satellite observations. *Journal of the Atmospheric Sciences*, *66*(1), 199–208. doi:

10.1175/2008jas2746.1

Mapes, B., & Neale, R. (2011). Parameterizing convective organization to escape the entrainment dilemma. *Journal of Advances in Modeling Earth Systems*, *3*(2). doi: 10.1029/2011MS000042

Mapes, B., Tulich, S., Lin, J., & Zuidema, P. (2006). The mesoscale convection life cycle: Building block or prototype for large-scale tropical waves? *Dynamics of Atmospheres and Oceans*, *42*(1-4), 3–29. doi: 10.1016/j.dynatmoce.2006.03.003

Martin, S. T., Artaxo, P., Machado, L., Manzi, A. O., Souza, R. A. F., Schumacher, C., ... Wendisch, M. (2017). The green ocean amazon experiment (GoAmazon2014/5) observes pollution affecting gases, aerosols, clouds, and rainfall over the rain forest. *Bulletin of the American Meteorological Society*, *98*(5), 981–997. doi: 10.1175/bams-d-15-00221.1

Martin, S. T., Artaxo, P., Machado, L. A. T., Manzi, A. O., Souza, R. A. F., Schumacher, C., ... Wendisch, M. (2016). Introduction: Observations and modeling of the green ocean amazon (GoAmazon2014/5). *Atmospheric Chemistry and Physics*, *16*(8), 4785–4797. doi: 10.5194/acp-16-4785-2016

Mayorga, E., Logsdon, M., Ballester, M., & Richey, J. (2012). *Lba-eco cd-06 amazon river basin land and stream drainage direction maps.* ORNL Distributed Active Archive Center. doi: 10.3334/ORNLDAAC/1086

Mlawer, E. J., Taubman, S. J., Brown, P. D., Iacono, M. J., & Clough, S. A. (1997). Radiative transfer for inhomogeneous atmospheres: RRTM, a validated correlated-k model for the longwave. *Journal of Geophysical Research: Atmospheres*, *102*(D14), 16663–16682. doi: 10.1029/97jd00237

Moncrieff, M. W., Waliser, D. E., Miller, M. J., Shapiro, M. A., Asrar, G. R., & Caughey, J. (2012). Multiscale convective organization and the YOTC virtual global field campaign. *Bulletin of the American Meteorological Society*, *93*(8), 1171–1187. doi: 10.1175/bams-d-11-00233.1

Morrison, H. (2003). Modeling clouds observed at SHEBA using a bulk microphysics parameterization implemented into a single-column model. *Journal of Geophysical Research*, *108*(D8). doi: 10.1029/2002jd002229

Morrison, H., Curry, J. A., & Khvorostyanov, V. I. (2005). A new double-moment microphysics parameterization for application in cloud and climate models. part i: Description. *Journal of the Atmospheric Sciences*, *62*(6), 1665–1677. doi: 10.1175/jas3446.1

Morrison, H., & Milbrandt, J. A. (2015). Parameterization of cloud microphysics based on the prediction of bulk ice particle properties. part i: Scheme description and idealized tests. *Journal of the Atmospheric Sciences*, *72*(1), 287–311. doi: 10.1175/jas-d-14-0065.1

NOAA National Centers for Environmental Information. (2022). *ETOPO 2022 15 arc-second global relief model.* NOAA National Centers for Environmental Information. doi: 10.25921/FD45-GT74

Powell, S. W. (2022). Criticality in the shallow-to-deep transition of simulated tropical marine convection. *Journal of the Atmospheric Sciences*, *79*(7), 1805 - 1819. doi: 10.1175/JAS-D-21-0155.1

Rodell, M., Houser, P. R., Jambor, U., Gottschalck, J., Mitchell, K., Meng, C.-J., ... Toll, D. (2004). The global land data assimilation system. *Bulletin of the American Meteorological Society*, *85*(3), 381–394. doi: 10.1175/bams-85-3-381

Schaefer, C., Lima, H., Teixeira, W., Jr, J., Souza, K., Corrêia, G., ... Ruivo, M. (2017). Solos da região amazônica. In N. C. Curi (Ed.), *Pedologia: solos dos biomas brasileiros.* Viçosa: Sociedade Brasileira de Ciência do Solo.

Schiro, K. A., Ahmed, F., Giangrande, S. E., & Neelin, J. D. (2018). GoAmazon2014/5 campaign points to deep-inflow approach to deep convection across scales. *Proceedings of the National Academy of Sciences*, *115*(18), 4577–4582. doi: 10.1073/pnas.1719842115

Schiro, K. A., & Neelin, J. D. (2019). Deep convective organization, moisture vertical structure, and convective transition using deep-inflow mixing. *Journal of the Atmospheric Sciences*, *76*(4), 965 - 987. doi: 10.1175/JAS-D-18-0122.1

Schiro, K. A., Neelin, J. D., Adams, D. K., & Lintner, B. R. (2016). Deep convection and column water vapor over tropical land versus tropical ocean: A comparison between the amazon and the tropical western pacific. *Journal of the Atmospheric Sciences*, *73*(10), 4043–4063. doi: 10.1175/jas-d-16-0119.1

Schumacher, C., & Funk, A. (2018). *Goamazon2014/5 rain rates from the sipam manaus s-band radar.* Atmospheric Radiation Measurement (ARM) Archive, Oak Ridge National Laboratory (ORNL), Oak Ridge, TN (US). doi: 10.5439/1459578

Sherwood, S. C., Bony, S., & Dufresne, J.-L. (2014). Spread in model climate sensitivity traced to atmospheric convective mixing. *Nature*, *505*(7481), 37–42. doi: 10.1038/nature12829

Silva Dias, M. A. F., Rutledge, S., Kabat, P., Silva Dias, P. L., Nobre, C., Fisch, G., ... Gatti, L. (2002). Cloud and rain processes in a biosphere-atmosphere interaction context in the amazon region. *Journal of Geophysical Research: Atmospheres*, *107*(D20), LBA 39-1-LBA 39-18. doi: 10.1029/2001JD000335

Stevens, B., & Bony, S. (2013). What are climate models missing? *Science*, *340*(6136), 1053–1054. doi: 10.1126/science.1237554

Tang, S., Xie, S., Zhang, Y., Zhang, M., Schumacher, C., Upton, H., ... Thieman, M. (2016). Large-scale vertical velocity, diabatic heating and drying profiles associated with seasonal and diurnal variations of convective systems observed in the GoAmazon2014/5 experiment. *Atmospheric Chemistry and Physics*, *16*(22), 14249–14264. doi: 10.5194/acp-16-14249-2016

Tian, Y., Zhang, Y., Klein, S. A., & Schumacher, C. (2021). Interpreting the diurnal cycle of clouds and precipitation in the ARM GoAmazon observations: Shallow to deep convection transition. *Journal of Geophysical Research: Atmospheres*, *126*(5), e2020JD033766. doi: 10.1029/2020JD033766

Vilà-Guerau de Arellano, J., Wang, X., Pedruzo-Bagazgoitia, X., Sikma, M., Agustí-Panareda, A., Boussetta, S., ... Gerken, T. (2020). Interactions between the amazonian rainforest and cumuli clouds: A large-eddy simulation, high-resolution ECMWF, and observational intercomparison study. *Journal of Advances in Modeling Earth Systems*, *12*(7), e2019MS001828. doi: 10.1029/2019MS001828

Waite, M. L., & Khouider, B. (2010). The deepening of tropical convection by congestus preconditioning. *Journal of the Atmospheric Sciences*, *67*(8), 2601–2615. doi: 10.1175/2010jas3357.1

Wu, C.-M., Stevens, B., & Arakawa, A. (2009). What controls the transition from shallow to deep convection? *Journal of the Atmospheric Sciences*, *66*(6), 1793–1806. doi: 10.1175/2008jas2945.1

Zhang, C., Gottschalck, J., Maloney, E. D., Moncrieff, M. W., Vitart, F., Waliser, D. E., ... Wheeler, M. C. (2013). Cracking the MJO nut. *Geophysical Research Letters*, *40*(6), 1223–1230. doi: 10.1002/grl.50244

Zhuang, Y., Fu, R., Marengo, J. A., & Wang, H. (2017). Seasonal variation of shallow-to-deep convection transition and its link to the environmental conditions over the central amazon. *Journal of Geophysical Research: Atmospheres*, *122*(5), 2649–2666. doi: 10.1002/2016jd025993